BIOCHEMISTRY
including biophysical chemistry & molecular biology

Article

pubs.acs.org/biochemistry

Origin of Product Selectivity in a Prenyl Transfer Reaction from the Same Intermediate: Exploration of Multiple FtmPT1-Catalyzed Prenyl Transfer Pathways

Li-Li Pan,[†,‡] Yue Yang,[§] and Kenneth M. Merz, Jr.*[,†,‡]

[†]Quantum Theory Project and Department of Chemistry, University of Florida, Gainesville, Florida 32611, United States

[‡]Institute for Cyber Enabled Research, Department of Chemistry, and Department of Biochemistry and Molecular Biology, Michigan State University, 578 South Shaw Lane, East Lansing, Michigan 48824, United States

[§]Biosciences and Biotechnology Division, Lawrence Livermore National Laboratory, 7000 East Avenue, Livermore, California 94550, United States

Supporting Information

ABSTRACT: FtmPT1 is a fungal indole prenyltransferase that catalyzes the reaction of tryptophan derivatives with dimethylallyl pyrophosphate to form various biologically active compounds. Herein, we describe detailed studies of FtmPT1 catalysis involving dimethylallyl pyrophosphate and Brevianamide F following the native pathway (yielding Tryprostatin B) and an alternate pathway observed in the Gly115Thr mutant of FtmPT1 yielding a novel cyclized product. Importantly, these two products arise from the same intermediate state, meaning that a step other than the cleavage of the dimethylallyl pyrophosphate (DMAPP; C−O) bond is differentiating between the two product reaction channels. From detailed potential of mean force (PMF) and two-dimensional PMF analyses, we conclude that the rate-limiting step is the cleavage of the C−O bond in DMAPP, while the deprotonation/cyclization step determines the final product distribution. Hence, in the case of FtmPT1, the optimization of the necessary catalytic machinery guides the generation of the final product after formation of the intermediate carbocation.

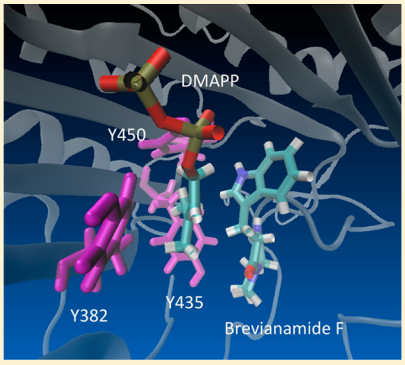

Prenyl transfer reactions are ubiquitous in nature and are utilized by organisms to generate a wide range of biologically active small molecules.[1−4] The fungal indole prenyltransferases (indole PTs) are a unique example of this class of enzyme. They differentiate themselves from other PTs by not requiring metal cofactors such as Mg^{2+} and Zn^{2+} to affect the prenyl transfer reaction, nor do they require the (N/D)DxxD motif seen in other PTs for binding or catalysis.[5−22] However, the "$\alpha\beta\beta\alpha$" duplicate chain order rule for α helices and β strands is satisfied in this class of PTs.[20] Recently, a number of experimental papers on fungal indole PTs exploring their regioselectivity have been published.[23−26] Multiple reaction channels are possible, so the fundamental question is how one reaction channel is favored over another by the characteristics of the active site of the protein catalyst involved. Importantly, once the C−O bond in DMAPP is cleaved, the dimethylallyl carbocation can react at one of two ends of the molecule: the less sterically crowded C5 position or the more crowded C2 site (see Figure 1). Indeed, both product types are observed, and the fundamental question of how formation of a sterically more crowded product can be favored over a less crowded reaction channel by active site characteristics arises. Both pathways yield interesting molecules, so the ultimate goal is to tune one pathway over another to synthesize the more desirable product. Figure 1 shows, as an example, the possible reaction products for the reaction of Brevianamide F and DMAPP as catalyzed by FtmPT1.

As shown in Figure 2, FtmPT1 is a PT whose polypeptide chain sequence is $\alpha\alpha\alpha\beta\beta\alpha\alpha\alpha\beta\beta\alpha\alpha\alpha-\beta\beta\alpha\alpha\beta\beta\alpha\alpha\beta\beta$, which satisfies the indole PT's "$\alpha\beta\beta\alpha$" motif. Produced by *Aspergillus fumigatus*, this fungal indole prenyltransferase catalyzes the reaction between dimethylallyl pyrophosphate (DMAPP) and L-Trp derivatives. Specifically, in this enzyme, the reaction of DMAPP with Brevianamide F (*cyclo*-L-Trp-L-Pro) to form the cell growth-inhibiting compound Tryprostatin B has been investigated.[12] Via biochemical and X-ray crystallographic techniques, Li et al.[12] identified two reaction channels for the prenyl transfer reaction between DMAPP and Brevianamide F: a C5−C8 reaction between the C5@DMAPP and the C8@indole for the wild-type enzyme and a C2−C9 reaction between the C2@DMAPP and the C9@indole for the Gly115Thr mutant (the C5−C8 is seen in the mutant, but as a side reaction). The native reaction channel produces Tryprostatin B, while the Gly115Thr mutant produces a product not seen in the native enzyme (see Figure 1). Further studies, regarding the regioselectivity of FtmPT1, have been

Received: June 13, 2014
Revised: September 3, 2014
Published: September 4, 2014

   dx.doi.org/10.1021/bi500747z | *Biochemistry* 2014, 53, 6126−6138

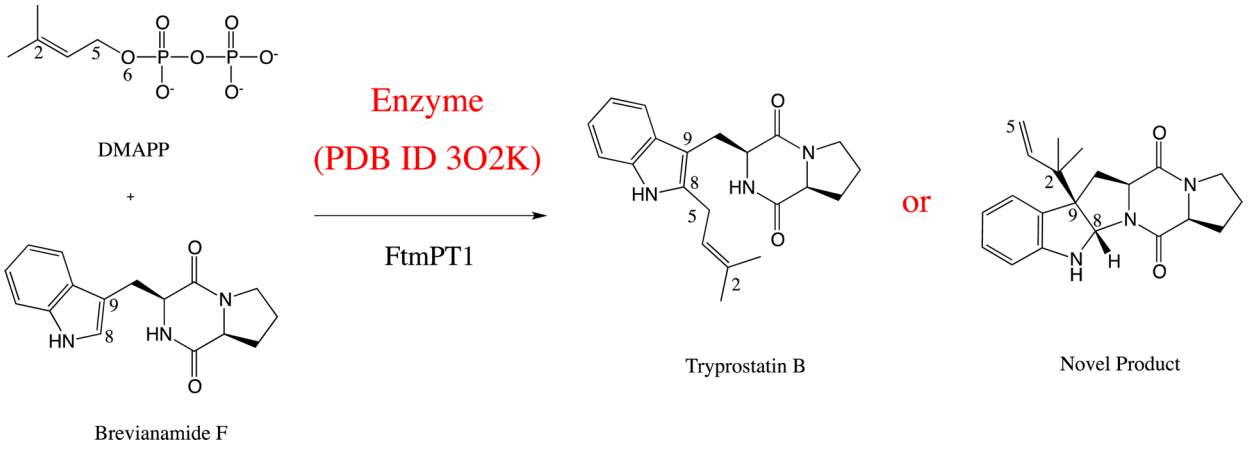

Figure 1. Catalytic mechanism hypotheses for the reaction between DMAPP and Brevianamide F catalyzed by FtmPT1: (a) C5−C8 and (b) C2−C9 reaction channels.

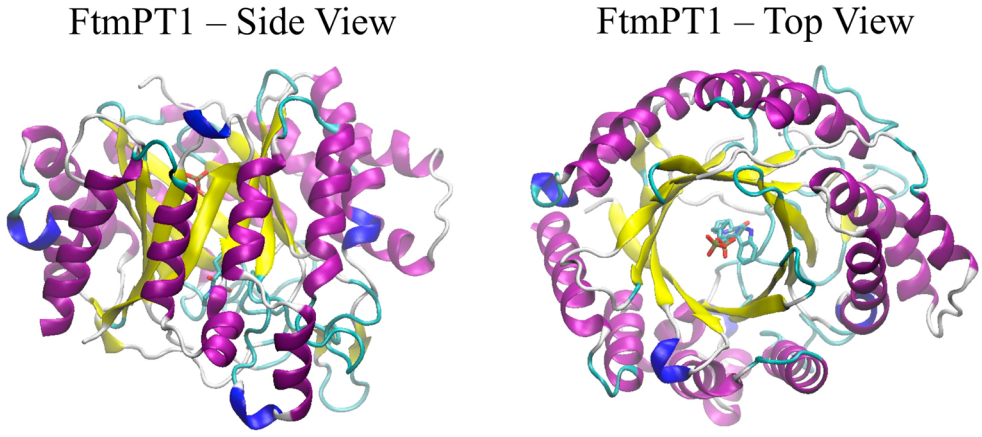

Figure 2. General view of the FtmPT1 complex system. Purple ribbons represent α-helices, yellow bands β strands, and green and white tubes loops. The licorice structures in the center of the binding site represent the substrates DMAPP and Brevianamide F.

reported.[25,26] Furthermore, nonaromatic carbon atoms can be prenylated along with aromatic carbon atoms on indole rings.[24] All these experimental papers demonstrate various regioselectivities observed in FtmPT1, making it a promising enzyme for the formation of novel products of value to the pharmaceutical industry.

Given the interesting behavior of this reaction and its sensitivity to point mutations, we decided to gain further insight into the catalytic mechanism of native FtmPT1 by studying the reaction between Brevianamide F and DMAPP. The reaction pathway consists of the prenyl transfer step, which is then followed by a proton transfer step and substrate loss to complete the reaction process. According to Li et al., besides the C5−C8 regioselectivity for the wild-type enzyme, and C2−C9 for the G115T mutant (with a decrease in product yield of 80%), they hypothesize that Glu102 is the proton acceptor for the deprotonation step in the reaction. Given the bifurcation in the preferred reaction channel between the native and mutant proteins, we decided to determine what was blocking the C2−C9 reaction channel in the native protein (see Figure 1) using modern theoretical tools. To reach this goal, we hypothesized an initial reaction mechanism for both the C2−C9 and C5−C8 reaction pathways, as shown in Figure 3. Our goal was to elucidate three important aspects of FtmPT1 catalysis: (1) elucidate the energetics of the C5−C8 and C2−C9 reaction channels in the wild-type enzyme, (2) identify the proton acceptors in the active site be it Glu102, surrounding water molecules, or another residue in the active site region, and (3) identify the prenylation reaction as being an S_N1 or S_N2 process, with the former involving a free carbocation. Herein, we describe the results of detailed quantum mechanical/molecular mechanical (QM/MM) studies of the catalytic mechanism of FtmPT1.

METHODS

General Features. All molecular dynamics simulations were performed in the assisted model building with energy refinement (AMBER, version 11) molecular dynamics package.[27] The crystal structures of FtmPT1 in complex with dimethylallyl *S*-thiolodiphosphate ($C_5H_{14}O_6P_2S$) and Brevianamide F ($C_{16}H_{17}N_3O_2$) were used as the starting geometry [Protein Data Bank (PDB) entry 3O2K].[12] The PDB structure was modified by replacing sulfur with oxygen in dimethylallyl *S*-thiolodiphosphate to form dimethylallyl pyrophosphate. Using the LEaP module of AMBER, hydrogen atoms were added to the structure.

The complex system was then solvated in a truncated octahedral cell with TIP3P[28] explicit water molecules. The ff99sb force field[29] was employed for the protein system, and the generalized Amber force field (GAFF)[30] was used for the substrate molecules to construct the parameter topology files. In all QM/MM molecular dynamics (MD) simulations, unless

dx.doi.org/10.1021/bi500747z | *Biochemistry* 2014, 53, 6126−6138

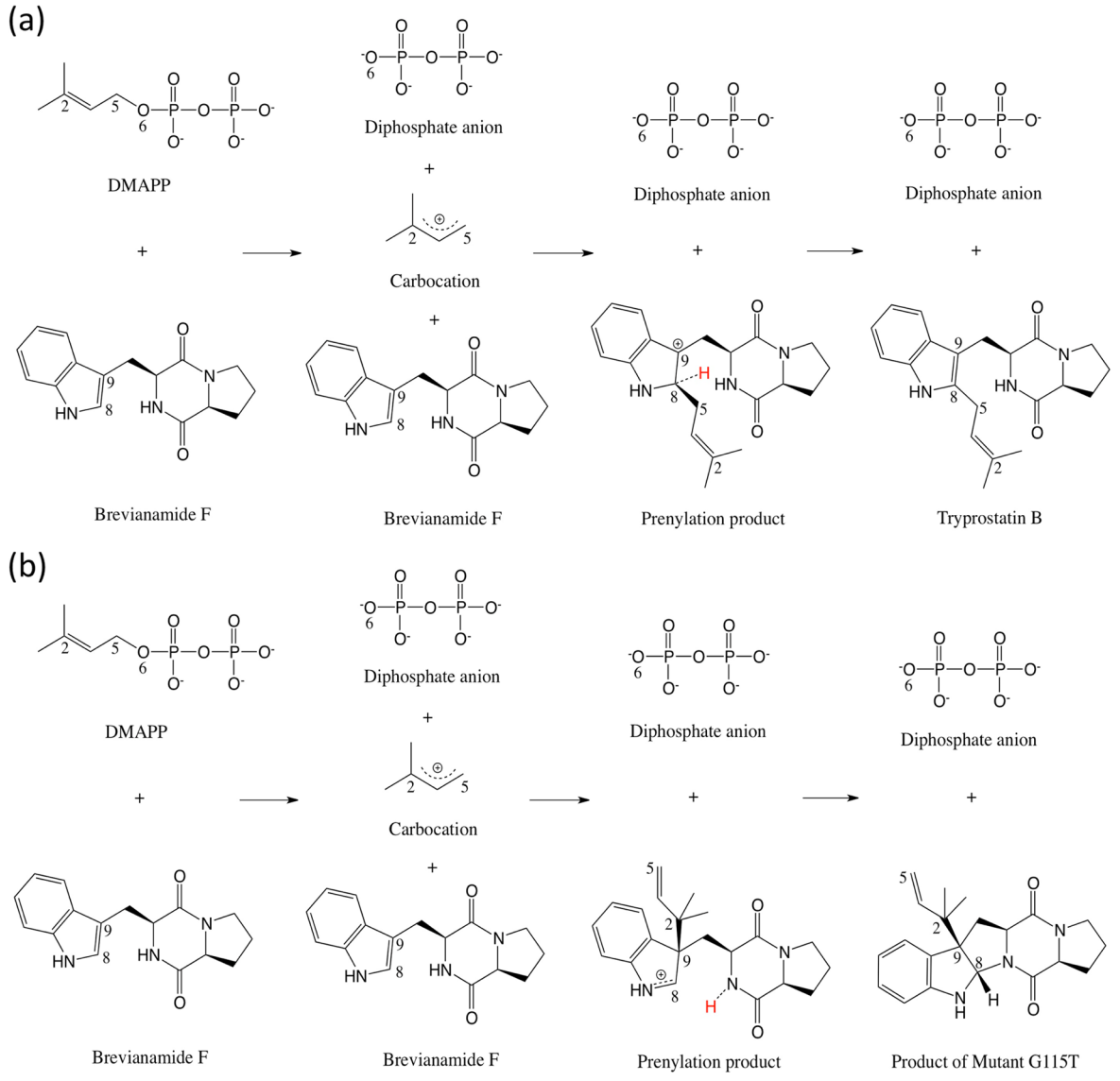

Figure 3. Hypothesized reaction mechanisms for complete reactions in FtmPT1 between DMAPP and Brevianamide F of (a) C5−C8 and (b) C2−C9 selections.

otherwise noted, we used the self-consistent charge density functional tight binding (SCC-DFTB) method,[31] as implemented in AMBER11. This approach has worked well in the past for prenylation-type reactions[32−35] among other reaction types and allows us to conduct extensive sampling along the reaction pathways. The charges for the substrate molecules were determined according to the restrained electrostatic potential (RESP) methodology[36] by a prior structure optimization at the M06L/6-31+G(d,p) level of theory with a subsequent electrostatic potential calculation at the HF/6-31+G(d,p) levels of theory using the Gaussian09 electronic structure program,[37] and the Antechamber module in the AMBERTools suite of programs. Long-range electrostatic interactions were treated with the particle mesh Ewald (PME) method,[38−41] and 8.0 Å cutoffs were used for the nonbonded interactions. All bonds with hydrogen atoms were constrained using SHAKE[42,43] except those included in the QM region for the calculations on the proton transfer step.

The entire system was initially minimized to remove close contacts using weak restraints. The system temperature was gradually increased to 300 K over 50 ps using a restrained MD simulation with a 1 fs time step. Then the restraints were slowly removed prior to a constant *NPT* 450 ps MD run. The SANDER module[44,45] was used for the minimization step and the 500 ps MD runs. The following 22 ns constant *NVT* MD simulation was subsequently finished using the PMEMD program. During the 22 ns production run, a 2 fs time step was used and snapshots were saved every 2 ps. The 1 ns product equilibration was completed using a similar procedure of initial minimization using the QM/MM MD capabilities in SANDER. The corresponding reactive substrate molecules, residues, and relevant water molecules were included in the QM region.

Visual Molecular Dynamics (VMD)[46,47] was used for structure analysis. GNUPlot[48] was used for all free energy profile (FEP) plots.

Prenyl Transfer Reaction Calculations. *C5−C8 Bond Formation.* QM/MM MD studies were used to obtain two-dimensional (2D) free energy profiles in which DMAPP and Brevianamide F were in the QM region. In the C5−C8 case, the two reaction coordinates were bond cleavage along the C5−O6 axis and bond formation along the C5−C8 axis. For

dx.doi.org/10.1021/bi500747z | *Biochemistry* 2014, 53, 6126−6138

C5−C8 bond formation, steered molecular dynamics (SMD)[49−53] was first applied to propagate the trajectory along the reaction coordinate, covering a bond distance range from 5.3 to 1.4 Å at an interval of 0.1 Å, using a force constant of 5000 kcal mol^{-1} Å^{-2}) and a pulling speed of 0.02 Å/ps. A 2D umbrella sampling was performed using as starting structures the C5−C8 SMD snapshots at the corresponding C5−C8 distances. We next propagated along the C5−O6 axis at an interval of 0.1 Å, resulting in 2040 windows within a C5−C8 region bound by [1.4 Å, 5.3 Å] and a C5−O6 region bound by [1.4 Å, 6.4 Å]. An initial 50 ps constant *NVT* equilibration was followed by another 50 ps constant *NVT* production run, during which the data were collected. The force constants for C5−C8 and C5−O6 bonds were 500−600 and 300−500 kcal mol^{-1} Å^{-2}, where the larger force constants were used for the higher-energy regions to ensure thorough sampling at the desired location of the 2D surface. The 2D weighted histogram analysis method (WHAM-2D)[54] was used to analyze the probability density and obtain the free energy profiles (FEP, 2D) for the unbiased system along the two reaction coordinates. For all of the steered MD and umbrella sampling calculations, unless otherwise indicated, a time step of 1 fs was used.

In addition to the 2D umbrella sampling simulations, one-dimensional (1D) umbrella sampling simulations were also performed for both C5−C8 and C5−O6 as single-reaction pathways. Starting structures of the corresponding umbrella sampling simulations were extracted from the corresponding steered MD trajectories at an interval of 0.1 Å between adjacent windows for both the O5−C6 and C5−C8 reaction coordinates in the 1D PMF calculations. The C5−C8 distance decreased from 5.3 to 1.4 Å, while the O6−C5 distance increased from 1.4 to 4.6 Å, resulting in 40 windows for the C5−C8 reaction coordinate and 33 windows for the O6−C5 reaction coordinate. Each of the windows was first equilibrated for 100 ps under *NVT* simulation conditions and then followed by a 150 ps production *NVT* simulation, during which the data were collected. The 1D weighted histogram analysis method (WHAM) was implemented to analyze the probability density and obtain the free energy profiles (FEP, 1D) for the unbiased system along the corresponding reaction coordinates.

C2−C9 Bond Formation. Carbon−carbon bond formation at C2−C9 was also examined using both 1D PMF and 2D PMF calculations. As in our studies outlined in C5−C8 Bond Formation, the C2−C9 reaction coordinate was mapped out using steered MD simulations with an interval of 0.1 Å between adjacent windows covering a distance interval of [4.5 Å, 1.4 Å]. The 1D PMF profile for C2−C9 bond formation was created using equilibration for 100 ps and sampling for 150 ps along the C2−C9 distance interval of [4.5 Å, 1.4 Å]. The 2D profile was generated using constant *NVT* equilibration for 50 ps and constant *NVT* sampling for 50 ps using a C2−C9 distance region of [4.5 Å, 1.4 Å] and for C5−O6 a distance interval of [1.4 Å, 6.4 Å], again resulting in 2040 windows. The force constant used for the steered MD studies was 5000 kcal mol^{-1} Å^{-2} with a pulling speed of 0.02 Å/ps. For the 1D and 2D PMF simulations, the force constants were 500−600 kcal mol^{-1} Å^{-2} for C2−C9 and 300−500 kcal mol^{-1} Å^{-2} for C5−O6, with the higher value being used in higher-energy regions of the profiles. The QM region employed included DMAPP and Brevianamide F.

Final Product Formation. *Proton Transfer To Form the Final Product for the C5−C8 Reaction Pathway.* The reaction system required a proton transfer step to remove the hydrogen atom connected to C8 on the indole ring of Brevianamide F after the C5−C8 prenylation step to produce the final product (Tryprostatin B). First, we needed to locate the minimum for the intermediate state by varying the distance between the diphosphate anion and the carbocation of the prenylation product using umbrella sampling. Starting from the protonated prenylation product, an umbrella sampling calculation was conducted for the C5−O6 distance, covering an interval of [6.0 Å, 15.0 Å] at 0.25 Å increments with a force constant of 100 kcal mol^{-1} Å^{-2}. Because this calculation was for the nonreactive pathway, the sampling was conducted using classical MD under *NVT* conditions using a time step of 1 fs, with a 1 ns equilibration stage followed by a 1 ns data collection step. This simulation was conducted to energetically characterize the prenylation product minimum. This free energy profile is given in Figure 6 of the Supporting Information.

From the end of the prenylation reaction, we conducted a 20 ns constant *NTP* MD equilibration of the protonated prenylation product complex followed by a 1 ns constant *NVT* QM/MM MD equilibration prior to the subsequent QM/MM steered MD and umbrella sampling steps. The position of the minima arising from these simulations versus the classical PMF simulations described above is given in Figure 6 of the Supporting Information.

Via analysis of the system after MD equilibration, the only two possible receptors of the proton were Glu102 and the water molecule adjacent to this residue. Hence, we included the side chain of Glu102 as well as the water molecule in the QM region, together with the protonated C5−C8 prenylation product. The diphosphate anion was not included in the QM region for this step. The steered MD and umbrella sampling calculations for the H(@C8)−C8 bond cleavage covered a distance interval of [1.1 Å, 3.5 Å]. The force constant for the steered MD study was 5000 kcal mol^{-1} Å^{-2} with a pulling speed of 0.02 Å/ps. For the umbrella sampling calculations, the force constant was 300 kcal mol^{-1} Å^{-2} for regions before and after windows in the transition state region, 600 kcal mol^{-1} Å^{-2} for windows close to the transition state, and 100 kcal mol^{-1} Å^{-2} for windows far from the transition state. WHAM-1D was used afterward to obtain the 1D FEP curve for this deprotonation step.

Cyclization and Deprotonation To Form the Final Product for the C2−C9 Reaction Pathway. An extra cyclization step via C8−N7 bond formation coupled with a proton transfer step via H(@N7)−N7 bond breakage was required to obtain the final product for the C2−C9 prenylation reaction pathway. As in the C5−C8 deprotonation step study, only a neighboring water molecule and the side chain of Glu102 as well as the C2−C9 prenylation product were included in the QM region. Starting from the protonated prenylation product, we created another 1D FEP curve using *NVT* MD umbrella sampling along the C5−O6 pathway over a distance increment of [6.0 Å, 15.0 Å] at intervals of 0.25 Å and a force constant of 100 kcal mol^{-1} Å^{-2}. This fully classical simulation was used to energetically characterize the minimum for this intermediate state.

We also simulated the prenylated C2−C9 system for 20 ns of MD simulation and 1 ns of QM/MM MD simulation (to generate the starting minimum for the subsequent QM/MM simulations) followed by a 1D steered MD study along the C8−N7 cyclization reaction pathway. The steered MD force constant was 5000 kcal mol^{-1} Å^{-2} with a pulling speed of 0.02 Å/ps. A 2D umbrella sampling study was conducted afterward

dx.doi.org/10.1021/bi500747z | *Biochemistry* 2014, 53, 6126−6138

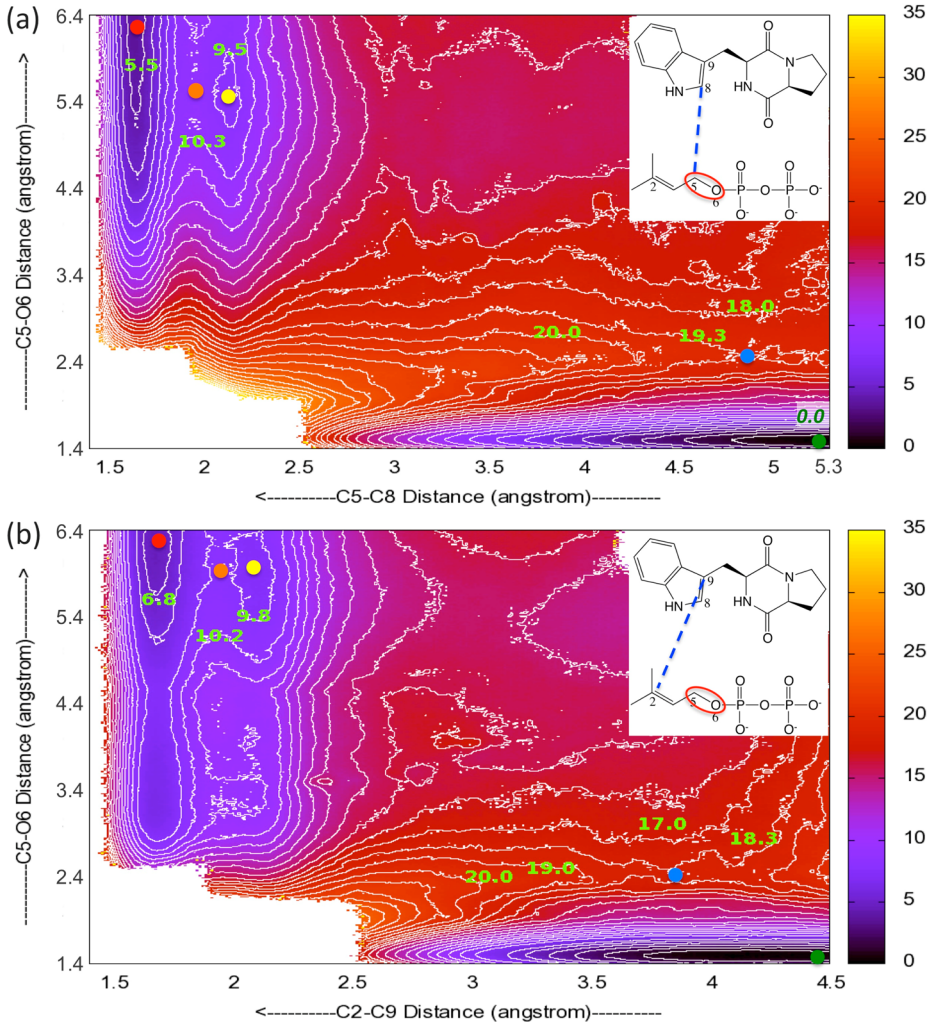

Figure 4. Free energy profiles (FEPs) in kilocalories per mole for (a) C5−C8 and (b) C2−C9 prenyl transfer steps. The free energies of starting states were set to zero. Map colors correspond to the energy scale shown to the right of the images. Lime-colored values represent free energies of iso-contour lines. Dots represent the stationary points for the reactions. Dots from right to left: starting state (green), first transition state (blue), intermediate state (yellow), second transition state (orange), and prenylation product (red), respectively.

using snapshots from the steered MD simulations for the C8−N7 reaction pathway as starting points. The H(@N7)−N7 distance was then varied, as well, resulting in 456 windows with a C8−N7 distance interval of [3.2 Å, 1.4 Å] and a N−H distance interval of [0.9 Å, 3.2 Å]. The force constants for C8−N7 bond formation were 300−500 kcal mol^{-1} Å^{-2}, and for the N−H bond cleavage, values between 500 and 1000 kcal mol^{-1} Å^{-2} were used. The higher force constants were used at windows close to the saddle points. WHAM-2D was used to obtain the final 2D profile.

Interaction Energy Decomposition. For the C5−C8 and C2−C9 prenylation reaction pathways, "π-chambers"[35,55−58] were used to encapsulate the carbocation intermediate states. The intermediate carbocations formed a cation−π interaction with the π-chamber, which was formed by phenol rings from three tyrosine residues in the active site region, Tyr382, Tyr435, and Tyr450. To quantitatively analyze the energies of interaction between each phenol ring and the carbocation, we used high-level QM calculations for the energy analysis. The calculations included only the formed carbocation and the three tyrosine residues. The backbones of the tyrosine residues were removed with only the phenol ring and the hydrogen-capped β-carbon being used in the subsequent calculations.

Five snapshots were picked from the umbrella sampling QM/MM MD simulation results at the intermediates states for both the C5−C8 and C2−C9 calculations. The reduced system of four aromatic fragments and the carbocation was first optimized at the M06L/6-31+G(d,p) level of theory, with all heavy atoms fixed. The optimization was then followed by a set of single-point calculations with basis set superposition error (BSSE) corrections to more quantitatively study the interactions between the carbocation and the π-chamber.

In addition, in the FtmPT1 active site, there are more residues that could affect the catalytic mechanism and the resulting product distribution. Hence, we used the energy decomposition method within the MM-GBSA module[59−62] in AMBER11 to analyze how the active site residues stabilize and destabilize the reactive species. Approximately 100 residues within 10 Å of the diphosphate anion, the dimethylallyl carbocation, and Brevianamide F were studied and analyzed via pairwise free energy decomposition. To facilitate this analysis, 42 ns *NVT* MD simulations of the starting, intermediate, and product states for the C5−C8 prenylation reaction were conducted to save snapshots for the analysis. Snapshots over the 42 ns MD were obtained every 50 ps for the MM-GBSA calculation.

dx.doi.org/10.1021/bi500747z | *Biochemistry* 2014, 53, 6126−6138

Table 1. Relative Free Energies (in kilocalories per mole) for Each State in the C5−C8 and C2−C9 Reaction Pathways[a]

		prenyl transfer step				proton transfer/cyclization step		
free energy (kcal/mol)	starting point	transition state 1	intermediate state	transition state 2	prenylation product	resting starting state	transition state 3	final product
C5−C8	0.0	19.3	9.2	10.0	5.3	−2.5	0.5	−20.8
C2−C9	0.0	18.5	9.5	10.0	6.5	0.8	16.8	−9.2

[a]Note that the energies of the starting states are set to zero.

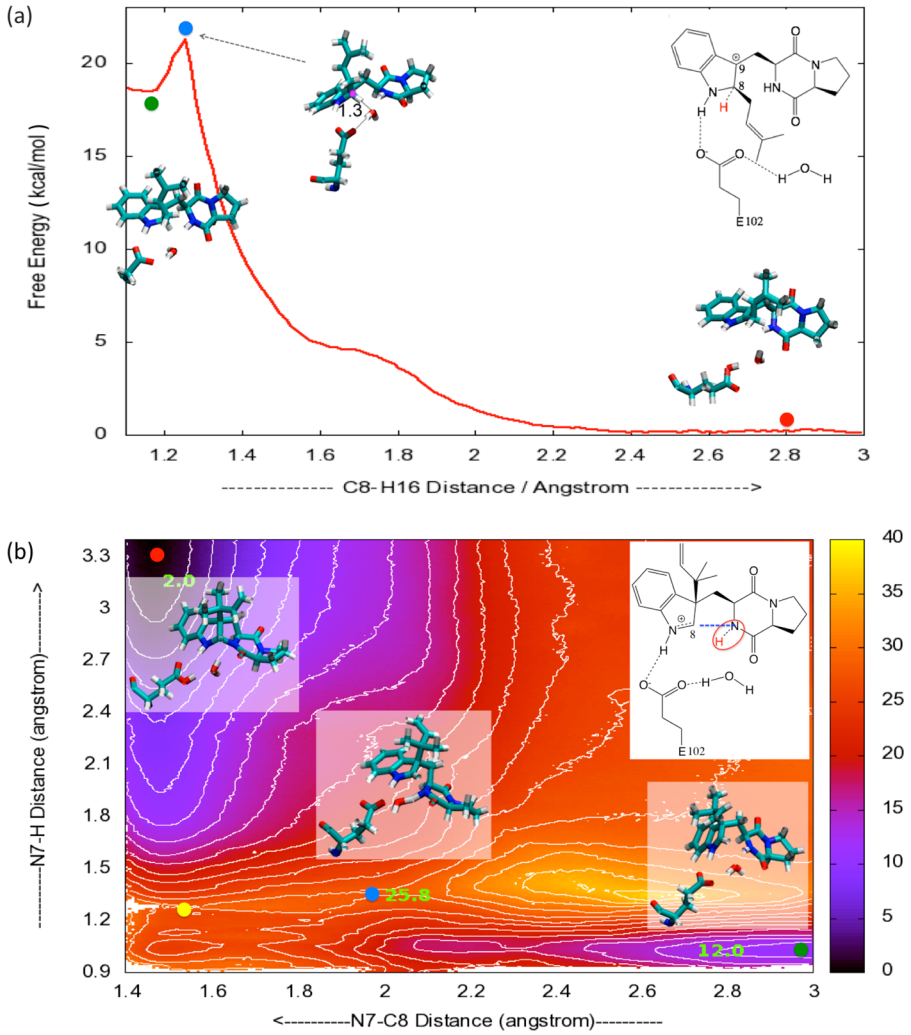

Figure 5. Free energy profiles (FEPs) in kilocalories per mole for (a) the proton transfer for the C5−C8 reaction pathway and (b) the deprotonation and cyclization steps for the C2−C9 reaction pathway. Map colors correspond to the energy scale shown at the right. Lime-colored values represent free energies of the iso-contour lines. Dots represent the key points for the reactions: starting state (green), transition state (blue), and final product (red). Note that for panel b the yellow dot also represents another potential transition state for the reaction.

RESULTS AND DISCUSSION

C5−C8 Reaction Pathway. *Prenyl Transfer Process.* Starting from a MD and QM/MM MD equilibrated staring complex, we conducted steered MD and umbrella sampling simulations to obtain the 2D free energy profiles (FEPs). Figure 4a shows the energy-contoured map for the corresponding FEP, with the C5−C8 distance as the *X*-axis and the C5−O6 distance as the *Y*-axis. From the figure, we can identify two saddle points and three wells, i.e., the starting state, two transition states, and one intermediate state, along with the product carbocation state. Starting at a C5−C8 distance of 5.25 Å and a C5−O6 distance of 1.42 Å, we proceed to the first transition state at a C5−C8 distance of 4.88 Å and a C5−O6 distance of 2.45 Å where the C5−O6 bond is initially broken. The next step for this reaction is the formation of the relatively stable dimethylallyl carbocation (DMA^+) at a C5−C8 distance of 2.15 Å and a C5−O6 distance of 5.45 Å. The carbocation is then attacked by C8 on the indole ring of Brevianamide F, yielding the second transition state of the reaction at a C5−C8 distance of 1.95 Å and a C5−O6 distance of 5.50 Å. The final prenylation product, which is the protonated form (@C8) of Tryprostatin B, is reached at a C5−C8 distance of 1.58 Å and a C5−O6 distance of 6.35 Å.

Other than the five states described above, no other local minima or saddle points could be identified for this reaction. Therefore, we conclude that this reaction follows an S_N1

dx.doi.org/10.1021/bi500747z | *Biochemistry* 2014, 53, 6126−6138

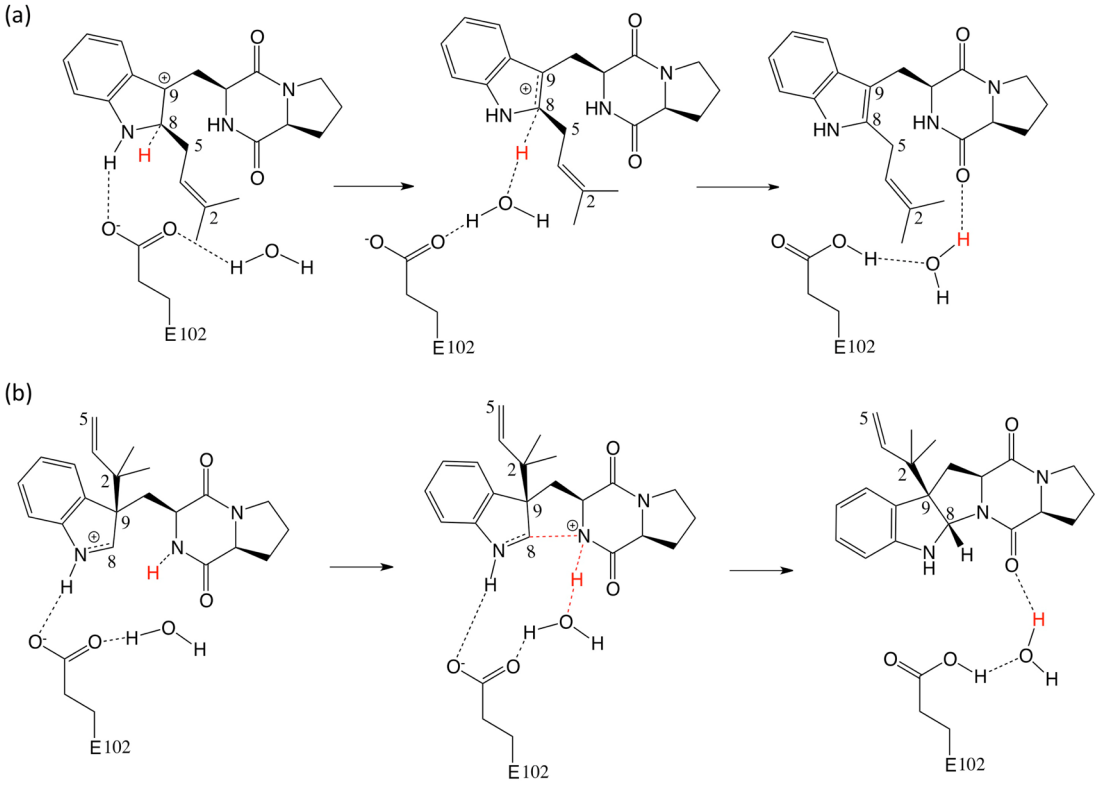

Figure 6. Reaction mechanisms for the proton transfer steps in the (a) C5−C8 and (b) C2−C9 reaction pathways.

reaction mechanism rather than an S_N2 reaction mechanism. The relative free energies are listed in Table 1. From this table, the rate-determining first transition state for C5−O6 bond cleavage has a relative free energy of 19.2 kcal/mol. This result matches the estimated experimental free energy barrier of 17.5 kcal/mol, which is approximated from its turnover rate of 5.57 s^{-1}.[12]

Proton Transfer Process. To obtain the final product, we need to deprotonate C8 from the protonated prenylation product. Prior to the deprotonation process, we estimate that the relaxation of the protonated prenylation product (with a C5−O6 distance of 6.35 Å) to the starting state of the deprotonation process (with a C5−O6 distance of 15.00 Å) has a free energy decrease of 7.8 kcal/mol (see Figure 6 of the Supporting Information). This energy decrease was also counted in the total reaction, as shown in Figure 7a and Table 1. For the deprotonation process, with both Glu102 and a nearby water molecule serving as proton acceptor candidates, we generated a 1D free energy profile for the deprotonation step along the H(@C8)−C8 reaction pathway, as shown in Figure 5a. From the figure, we find that the deprotonation process reaches a transition state at a H(@C8)−C8 distance of 1.25 Å with an energy barrier of 3.0 kcal/mol compared to the starting protonated state. The reaction reaches the product state at a H(@C8)−C8 distance of 2.4 Å with a free energy 18.3 kcal/mol lower than that of the starting state.

From the mechanisms shown in Figures 6a and 7a, the starting state for the protonated intermediate has two proton accepting groups: Glu102 and a water molecule. Initially, Glu102 forms a hydrogen bond with the nitrogen atom on the indole ring of the protonated prenylation product, and simultaneously forms another hydrogen bond with the water molecule. At the transition state, we find that the proton is initially transferred to the water molecule. Right after the transition state, the extra proton is transferred to the water molecule and then without activation to Glu102. Hence, Glu102 is the final transfer point for the proton as proposed,[12] but an intervening water molecule facilitates the transfer.

Final Product Equilibration. To observe the dynamics of the final product, Tryprostatin B, in the binding pocket of FtmPT1, we ran a 22 ns classical MD simulation. In the MD simulation, we found that the product remained bound in the active site with two different hydrogen bonding situations. Initially, the two original hydrogen bonds formed at the end of the proton transfer reaction remained; the water molecule, which was involved in the proton transfer, was forming a bridge between the oxygen atom on Tryprostatin B's six-membered ring and protonated Glu102 through two hydrogen bonds (see Figure 1a of the Supporting Information). In the later stages of the MD simulation, the water molecule escapes the active site and two other hydrogen bonds are formed: one from the protonated oxygen on Glu102 to the oxygen atom on Tryprostatin B's six-membered ring and the other from the oxygen atom on Glu102 to the nitrogen atom on Tryprostatin B's six-membered ring (see Figure 1b of the Supporting Information). At least at the short time scale of these simulations, Tryprostatin B remains in the active site of FtmPT1, and to observe product loss, lengthier simulations will be required.

C2−C9 Reaction Pathway. To understand the regioselectivity of native FtmPT1, we decided to examine the reaction pathway (C2−C9) that generates the product observed in the G115T mutant of FtmPT1. The initial steps in both the C5−C8 and C2−C9 pathways are identical (cleavage of the DMAPP C−O bond), so the origin of regioselectivity is another step in the reaction. From a study of the C2−C9

dx.doi.org/10.1021/bi500747z | *Biochemistry* 2014, 53, 6126−6138

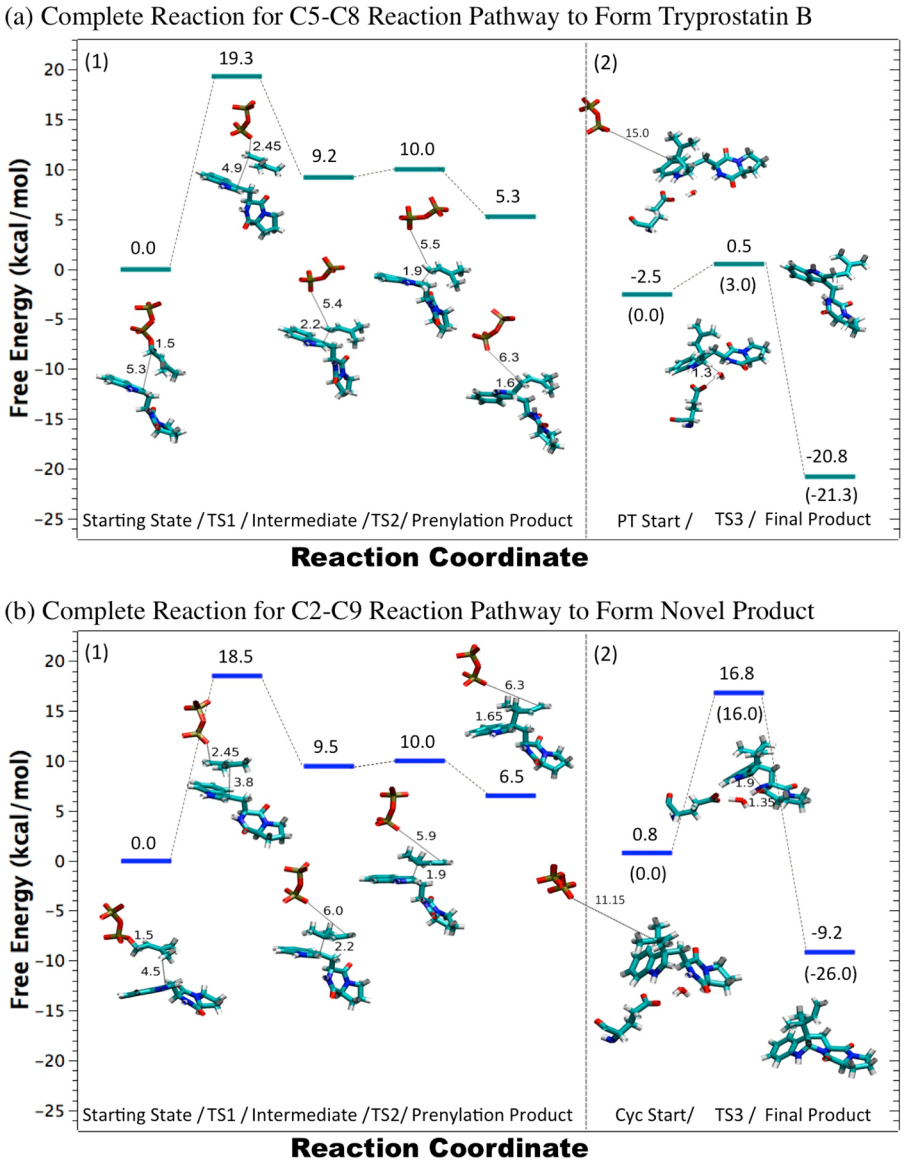

Figure 7. Complete reaction profiles with relative free energies and the associated structures for the C5−C8 and C2−C9 pathways: (1) prenyl transfer reaction and (2) proton transfer reaction. Distances for the relevant reaction coordinates are given on the structures. Free energies compared to the starting state are given above the green and blue lines. Note the energies in parentheses for the proton transfer step that are compared to their own starting state minima (for the diphosphate and prenylated carbocation). The starting state for reaction 2 (proton transfer) is the relaxed state of the product from reaction 1 (prenylation reaction).

pathway, we will garner insights into how the enzyme controls its product distribution once the carbocation intermediate is formed.

Prenyl Transfer Process. For the prenyl transfer part, the computed 2D free energy profile is given in Figure 4b. From this 2D FEP map, we find that the C2−C9 pathway is similar to the C5−C8 pathway. For the formation of the carbocation, the cleavage of the DMAPP C−O bond is again rate-limiting, while the resultant minima on the surface between C2−C9 and C5−C8 are very similar. Hence, the C2−C9 prenyl transfer reaction also follows an S_N1 reaction mechanism, which supports the mechanistic hypothesis depicted in Figure 3b. This means that the enzyme does not favor one product or another from a thermodynamic perspective along the pathway generating the appropriately positioned carbocation intermediate.

Looking into the details of the C2−C9 reaction pathway based on the 2D FEP shown in Figure 4b, we find that the reaction starts at a C2−C9 distance of 4.49 Å and a C5−O6 distance of 1.42 Å, with the first transition state at a C2−C9 distance of 3.81 Å and a C5−O6 distance of 2.45 Å, which cleaves the C5−O6 bond on DMAPP. A relatively stable dimethylallyl carbocation is formed reaching the intermediate state at a C2−C9 distance of 2.15 Å and a C5−O6 distance of 6.05 Å. The carbocation then forms a C−C bond with C9 on the indole ring of Brevianamide F via a second transition state at a C2−C9 distance of 1.95 Å and a C5−O6 distance of 5.95 Å. The final prenylation product, which is the protonated state of the novel product, was finally formed at a C2−C9 distance of 1.65 Å and a C5−O6 distance of 6.35 Å.

The energy barriers for each state are listed in Table 1. Compared to the C5−C8 prenylation reaction, we find that the first transition state has a similar free energy barrier of 18.5 kcal/mol with respect to the starting state. As noted above, this is because the first transition state involves the cleavage of only

dx.doi.org/10.1021/bi500747z | *Biochemistry* 2014, 53, 6126−6138

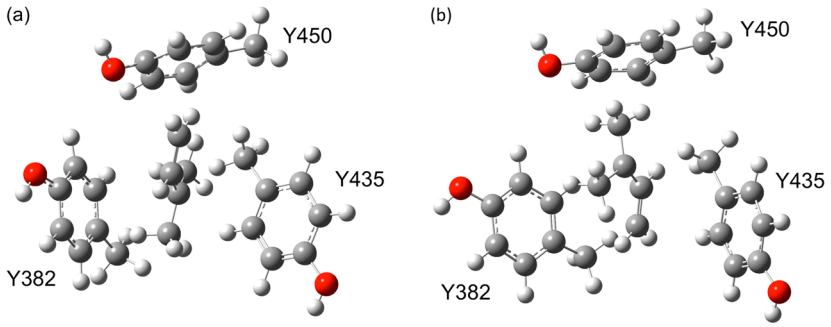

Figure 8. Truncated representations of the intermediate state π-chambers observed along the (a) C5−C8 prenylation and (b) C2−C9 prenylation pathways. The center fragment represents the carbocation, and the phenol fragments represent truncated tyrosine residues.

the C5−O6 bond on DMAPP and has nothing to do with C−C bond formation.

For C−C bond formation, the two free energy barriers for C2−C9 and C5−C8 are essentially identical at ∼10.0 kcal/mol with respect to the starting state. The free energy for the C5−C8 prenylated product (5.3 kcal/mol) was slightly lower than that of C2−C9 (6.5 kcal/mol). This is because the C2−C9 prenylated product is less stable because of steric effects associated with the formation of a highly substituted C−C bond (see Figure 3b).

Cyclization and Proton Transfer Process. Prior to the deprotonation process for the C2−C9 reaction pathway, similarly, we find that the relaxation from the protonated prenylation product (with a C5−O6 distance of 6.35 Å) to the deprotonation starting state (with a C5−O6 distance of 11.15 Å) involves a free energy decrease of 5.7 kcal/mol (see Figure 7 of the Supporting Information). This energy decrease was included for the total reaction, as shown in Figure 7b and Table 1.

For the deprotonation process, the C2−C9 reaction pathway was more complicated than the C5−C8 one, as the protonated prenylation product had to undergo another cyclization process in addition to the deprotonation step to yield the final product. The cyclization takes place via C8−N7 bond formation yielding a new five-membered ring between indole and the six-membered ring of Brevianamide F generating Tryprostatin B (see Figure 1). To fully characterize this pathway, we used a 2D FEP approach. A 2D graph is shown in Figure 5b with the C8−N7 distance as the *X*-axis and the H(@N7)−N7 distance as the *Y*-axis. From this 2D map, we were able to fully characterize the details of this deprotonation/cyclization process.

From the starting state at the bottom right with a C8−N7 distance of 3.0 Å and a H(@N7)−N7 distance of 1.0 Å, the transition state is reached at a C8−N7 distance of 2.05 Å and a H(@N7)−N7 distance of 1.27 Å, where both the N7−C8 bond is starting to be formed and the H(@N7)−N7 bond is starting to break. H@N7 then left N7 and transferred the extra proton to Glu102 by bridging of the water molecule close to them, while the final product was finally formed by formation of the N7−C8 bond with a distance of 1.55 Å. At this time, the H atom was 3.4 Å from N7. One more possibility for the transition state was observed at a C8−N7 distance of 1.65 Å and a H(@N7)−N7 distance of 1.25 Å. In both cases, the H(@N7)−N7 bond breaks and the proton ends up bound to Glu102 via an activationless transfer through the active site water molecule. The transition state free energy barrier for the first pathway is 16.0 kcal/mol, while for the second one, the free energy barrier is 16.5 kcal/mol. The two transition states are along a ridge between the starting state and the final product and differ by the amount by which the N7−C8 bond is formed, the former being longer than the latter. The first pathway is favored and will be used throughout the remaining discussion.

With the energy barriers listed in Table 1, we find that the rate-determining step for the C5−C8 and C2−C9 reaction pathways is the O−C bond cleavage step. Because the prenylation reactions for both pathways follow an S_N1 reaction mechanism and start from the same starting state, the O−C bond cleavage process should be identical as observed. The relative free energies for C5−C8 and C2−C9 prenylation pathways are also nearly identical. Hence, the final proton transfer/cyclization step determines the final product distribution. The cyclization/deprotonation step (16.8 kcal/mol) for the C2−C9 pathway has a barrier much higher than that for the C5−C8 deprotonation step (0.5 kcal/mol). Thus, once the intermediate prenylation product is formed, the C5−C8 pathway transitions to the product nearly without activation, while the C5−C8 pathway has a substantial barrier to overcome, which is higher than that of the intermediate state itself. Equilibration between C2−C9 and C5−C8 can then funnel away the C2−C9 pathway, yielding the exclusive C5−C8 product for the reaction.

Final Product Equilibration. To further explore the binding interactions for the C2−C9 product, we performed a 22 ns classical MD simulation. Hydrogen bonds between the active site water and Glh102 (protonated Glu) stabilized the final product within the active site where it remained over the relatively short time scale of the final classical MD simulation (see Figure 1c of the Supporting Information).

π-Chamber Binding Analysis. To further examine the interactions between the formed carbocation and the aromatic groups from the active site tyrosine residues during the prenyl transfer reaction, we conducted QM calculations (Figure 8), and the results are summarized in Table 2. From Table 2, we observe that Tyr435, which has a T-stacking interaction with the carbocation (see Figures 9b and 10b), contributed similar interaction energies to the C5−C8 (−9.81 kcal/mol) and C2−C9 (−9.67 kcal/mol) reaction pathways. Tyr382 had a −13.17

Table 2. π−Cation Interaction Energies (kilocalories per mole) for the Carbocation Intermediate States along the C5−C8 and C2−C9 Reaction Pathways

pathway	Y382	Y435	Y450
C5−C8	−13.17	−9.81	−12.57
C2−C9	−9.82	−9.67	−10.58

dx.doi.org/10.1021/bi500747z | *Biochemistry* 2014, 53, 6126−6138

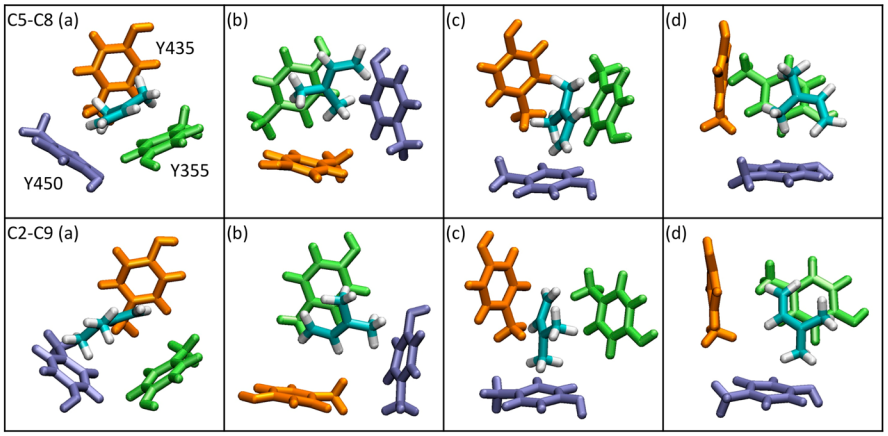

Figure 9. Truncated snapshots for intermediate state π-chambers observed along the C5−C8 and C2−C9 prenylation pathways. (a−d) Different views of the tyrosine phenol rings and the intermediate carbocation.

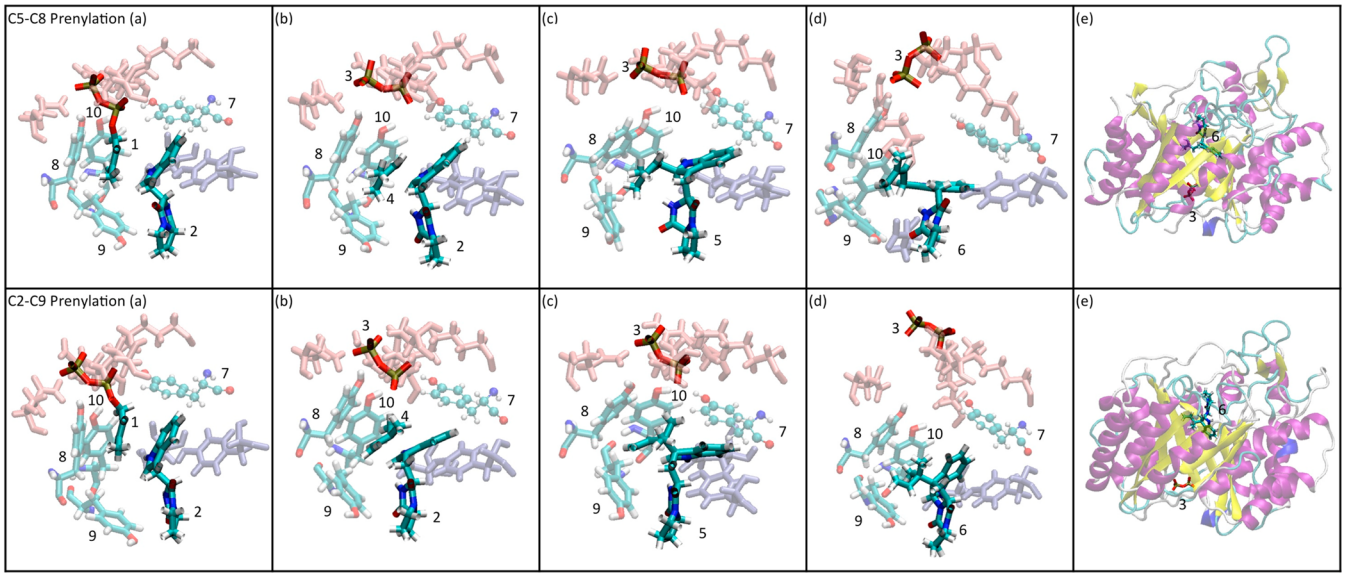

Figure 10. Snapshots from the wild-type FtmPT1 catalytic pathway along the C5−C8 and C2−C9 reaction pathways: (a) starting and/or resting state, (b) prenylation intermediate state, (c) prenylation product (intermediate) state, (d) final product, and (e) final product state inside FtmPT1. Numbers represent ligands and active site residues: (1) DMAPP, (2) Brevianamide F, (3) OPP, (4) DMA and carbocation, (5) protonated prenylation product, (6) final product, (7) Tyr205, (8) Tyr382, (9) Tyr435, and (10) Tyr450. Pink residues (Arg113, Lys201, Lys294, and Gln380) are hydrogen-bonded to the diphosphate anion; ice blue residues (Glu102 and Tyr205) are hydrogen-bonded to Brevianamide F.

kcal/mol interaction energy with the C5−C8 intermediate carbocation and a −9.82 kcal/mol interaction energy with the C2−C9 intermediate carbocation. Tyr450 contributed −12.57 kcal/mol to the C5−C8 intermediate carbocation and −10.58 kcal/mol to the C2−C9 intermediate carbocation. Both Tyr382 and Tyr450 had a >2.0 kcal/mol stronger interaction with the C5−C8 intermediate carbocation. In the case of Tyr450, the π-chamber placed the least substituted end of the carbocation into the face of this aromatic ring, while the C2−C9 intermediate placed the methyl groups from the more substituted end into the face of this aromatic ring. This placed more charge into the face of the rings for C5−C8 than for C2−C9, ultimately leading to a greater stabilization in this instance. For Tyr382, the situation is less obvious, but it does appear that the intermediate carbocation has a closer interaction with the aromatic ring of Tyr382, which might afford the differential stabilization that is observed.

To further study the factors stabilizing the phosphate dianion and the carbocation, we conducted an energy decomposition analysis. Figure 2 of the Supporting Information shows the four states involved in the C5−C8 pathway with their interacting residues and water molecules. From the figure, we observe that the diphosphate group is stabilized by hydrogen bonding interactions with the side chains of Arg113, Lys201, Tyr205, Gln380, Lys294, Tyr450, and nine crystal water molecules (not shown in the figure) in all states that were examined. It also reveals the reason for stabilization of the DMA^+ carbocation: the surrounding side chains of the tyrosine residues (Tyr201, Tyr382, Tyr435, and Tyr450) play an important role in stabilizing the carbocation from beginning to end via π−cation interactions. Specifically, at the intermediate state, Tyr382 was parallel to the carbocation, while Tyr435 and Tyr450 were perpendicular to the carbocation. These three residues are perfectly situated to stabilize of the carbocation. Table 1 of the Supporting Information also shows the decomposition free energies for these four tyrosine residues paired with the DMA^+ carbocation using MM-PBSA. The results show that the tyrosine residues have strong van de Waals interactions with

dx.doi.org/10.1021/bi500747z | *Biochemistry* 2014, 53, 6126−6138

the carbocation. Hence, all four tyrosine residues help to stabilize DMA^+ from bond cleavage to new bond formation.

CONCLUSION

We have successfully conducted QM/MM simulations to further elucidate the catalytic mechanism for the prenyltransferase reaction catalyzed by wild-type FtmPT1. We explored the reaction of Brevianamide F with DMAPP via the C5−C8 and C2−C9 reaction channels and found, as expected, that C5−C8 and C2−C9 had very similar activation parameters for the prenylation step. Hence, the final proton transfer/cyclization step was the product-determining step for these reactions, with the deprotonation of the C5−C8 intermediate being nearly without activation (0.5 kcal/mol), while the deprotonation process for the C2−C9 pathway had a substantial barrier (higher than the C5−C8 and C2−C9 intermediate states) of 16.8 kcal/mol, resulting in the exclusive formation of the wild-type product Tryprostatin B. A key feature of the final deprotonation step was the involvement of a bridging water molecule between the transferring proton and Glu102, which was found in both cases to be the proton receptor.

Via energy decomposition analysis, we assessed the stabilizing effects of active site tyrosine residues on the DMA^+ carbocation at the QM level. The surrounding tyrosine residues formed a π-chamber resulting in cation−π interactions between the formed carbocation intermediate and the π-chamber. The C5−C8 carbocation was stabilized 5.48 kcal/mol more than the C2−C9 carbocation intermediate. The origin of this is the placement of the methyl groups into the aromatic faces for the C2−C9 intermediate, while the hydrogen atoms from the primary end of the allyl cation are placed into the aromatic faces for C5−C8. Finally, the diphosphate anion leaving group was stabilized throughout by Arg113, Lys201, Tyr205, Gln380, Lys294, Tyr450, and nine crystal water molecules in the active site of FtmPT1.

ASSOCIATED CONTENT

Supporting Information

We provide binding site snapshots for each stable state, 1D FEPs for O−C bond cleavage and C5−C8 bond formation, 1D FEPs for the relaxation of the prenylation product, RESP charges of the carbocation, and a table of decomposition free energies contributed by tyrosine residues with respect to the stability of the carbocation. This material is available free of charge via the Internet at http://pubs.acs.org.

AUTHOR INFORMATION

Corresponding Author

*E-mail: kmerz1@gmail.com. Phone: (517) 355-9715. Fax: (517) 353-7248.

Funding

We acknowledge the financial support from National Institutes of Health Grants GM044974 and GM066859.

Notes

The authors declare no competing financial interest.

ACKNOWLEDGMENTS

We thank Dr. Michael Weaver for meaningful discussions on this topic. We also thank the high-performance computing center at the University of Florida (UFHPC) for providing and maintaining computational resources.

ABBREVIATIONS

MD, molecular dynamics; QM/MM, quantum mechanics/molecular mechanics; AMBER, assisted model building with energy refinement; SANDER, simulated annealing with NMR-derived energy restraints; WHAM, weighted histogram analysis method; rmsd, root-mean-square deviation; RESP, restrained electrostatic potential; GAFF, general Amber force field; PME, particle mesh Ewald; PT, prenyltransferase; DMAPP, dimethylallyl pyrophosphate; DMA^+, dimethylallyl carbocation; TS, transition state.

REFERENCES

(1) Gordon, L. B., Kleinman, M. E., Miller, D. T., Neuberg, D. S., Giobbie-Hurder, A., Gerhard-Herman, M., Smoot, L. B., Gordon, C. M., Cleveland, R., Snyder, B. D., Fligor, B., Bishop, W. R., Statkevich, P., Regen, A., Sonis, A., Riley, S., Ploski, C., Correia, A., Quinn, N., Ullrich, N. J., Nazarian, A., Liang, M. G., Huh, S. Y., Schwartzman, A., and Kieran, M. W. (2012) Clinical trial of a farnesyltransferase inhibitor in children with Hutchinson-Gilford progeria syndrome. *Proc. Natl. Acad. Sci. U.S.A. 109*, 16666−16671.

(2) Casey, P. J., and Seabra, M. C. (1996) Protein prenyltransferases. *J. Biol. Chem. 271*, 5289−5292.

(3) Spindler, S. R., Li, R., Dhahbi, J. M., Yamakawa, A., Mote, P., Bodmer, R., Ocorr, K., Williams, R. T., Wang, Y. S., and Ablao, K. P. (2012) Statin Treatment Increases Lifespan and Improves Cardiac Health in *Drosophila* by Decreasing Specific Protein Prenylation. *PLoS One 7*, e39581.

(4) Tantillo, D. J. (2010) The carbocation continuum in terpene biosynthesis: Where are the secondary cations? *Chem. Soc. Rev. 39*, 2847−2854.

(5) Amatore, C., Thiebault, A., and Verpeaux, J. N. (1989) Unexpected Single Electron-Transfer Catalyzed Cyclization of Prenyl Sulfone Dimer: Evidence for Radical-Anion Coupling in the Outer-Sphere Oxidation of Prenyl Sulfone Carbanion. *J. Chem. Soc., Chem. Commun.*, 1543−1545.

(6) Bonitz, T., Alva, V., Saleh, O., Lupas, A. N., and Heide, L. (2011) Evolutionary Relationships of Microbial Aromatic Prenyltransferases. *PLoS One 6*, e27336.

(7) Brajeul, S., Delpech, B., and Marazano, C. (2007) Sulfonium salts as prenyl, geranyl, and isolavandulyl transfer agents towards benzoylphloroglucinol derivatives. *Tetrahedron Lett. 48*, 5597−5600.

(8) Chen, A. J., Kroon, P. A., and Poulter, C. D. (1994) Isoprenyl Diphosphate Synthases: Protein-Sequence Comparisons, a Phylogenetic Tree, and Predictions of Secondary Structure. *Protein Sci. 3*, 600−607.

(9) Davisson, V. J., Neal, T. R., and Poulter, C. D. (1993) Farnesyl-Diphosphate Synthase: Catalysis of an Intramolecular Prenyl Transfer with Bisubstrate Analogs. *J. Am. Chem. Soc. 115*, 1235−1245.

(10) Heide, L. (2009) Prenyl transfer to aromatic substrates: Genetics and enzymology. *Curr. Opin. Chem. Biol. 13*, 171−179.

(11) Hong, B. C., Hong, J. H., and Tsai, Y. C. (1998) Regio- and enantioselective prenyl anion transfer: Application to the total synthesis of (−)-rosiridol. *Angew. Chem., Int. Ed. 37*, 468−470.

(12) Jost, M., Zocher, G., Tarcz, S., Matuschek, M., Xie, X. L., Li, S. M., and Stehle, T. (2010) Structure-Function Analysis of an Enzymatic Prenyl Transfer Reaction Identifies a Reaction Chamber with Modifiable Specificity. *J. Am. Chem. Soc. 132*, 17849−17858.

(13) Kuzuyama, T., Noel, J. P., and Richard, S. B. (2005) Structural basis for the promiscuous biosynthetic prenylation of aromatic natural products. *Nature 435*, 983−987.

(14) Li, S. M. (2009) Evolution of aromatic prenyltransferases in the biosynthesis of indole derivatives. *Phytochemistry 70*, 1746−1757.

(15) Liang, P. H., Ko, T. P., and Wang, A. H. J. (2002) Structure, mechanism and function of prenyltransferases. *Eur. J. Biochem. 269*, 3339−3354.

(16) Nurenberg, G., and Volmer, D. A. (2012) The analytical determination of isoprenoid intermediates from the mevalonate pathway. *Anal. Bioanal. Chem. 402*, 671−685.
(17) Poulter, C. D. (1996) Mechanistic studies of the prenyl transfer reaction with fluorinated substrate analogs. *Biomedical Frontiers of Fluorine Chemistry 639*, 158−168.
(18) Saleh, O., Haagen, Y., Seeger, K., and Heide, L. (2009) Prenyl transfer to aromatic substrates in the biosynthesis of aminocoumarins, meroterpenoids and phenazines: The ABBA prenyltransferase family. *Phytochemistry 70*, 1728−1738.
(19) Sinko, W., de Oliveira, C., Williams, S., Van Wynsberghe, A., Durrant, J. D., Cao, R., Oldfield, E., and McCammon, J. A. (2011) Applying Molecular Dynamics Simulations to Identify Rarely Sampled Ligand-bound Conformational States of Undecaprenyl Pyrophosphate Synthase, an Antibacterial Target. *Chem. Biol. Drug Des. 77*, 412−420.
(20) Tello, M., Kuzuyama, T., Heide, L., Noel, J. P., and Richard, S. B. (2008) The ABBA family of aromatic prenyltransferases: Broadening natural product diversity. *Cell. Mol. Life Sci. 65*, 1459−1463.
(21) Yu, X., Liu, Y., Xie, X. L., Zheng, X. D., and Li, S. M. (2012) Biochemical Characterization of Indole Prenyltransferases: Filling the Last Gap of Prenylation Positions by a 5-Dimethylallyltryptophan Synthase from *Aspergillus clavatus*. *J. Biol. Chem. 287*, 1371−1380.
(22) Yu, X., Xie, X. L., and Li, S. M. (2011) Substrate promiscuity of secondary metabolite enzymes: Prenylation of hydroxynaphthalenes by fungal indole prenyltransferases. *Appl. Microbiol. Biotechnol. 92*, 737−748.
(23) Wollinsky, B., Ludwig, L., Xie, X. L., and Li, S. M. (2012) Breaking the regioselectivity of indole prenyltransferases: Identification of regular C3-prenylated hexahydropyrrolo[2,3-b]indoles as side products of the regular C2-prenyltransferase FtmPT1. *Org. Biomol. Chem. 10*, 9262−9270.
(24) Chen, J., Morita, H., Wakimoto, T., Mori, T., Noguchi, H., and Abe, I. (2012) Prenylation of a Nonaromatic Carbon of Indolylbutenone by a Fungal Indole Prenyltransferase. *Org. Lett. 14*, 3080−3083.
(25) Luk, L. Y. P., Qian, Q., and Tanner, M. E. (2011) A Cope Rearrangement in the Reaction Catalyzed by Dimethylallyltryptophan Synthase? *J. Am. Chem. Soc. 133*, 12342−12345.
(26) Mahmoodi, N., and Tanner, M. E. (2013) Potential Rearrangements in the Reaction Catalyzed by the Indole Prenyltransferase FtmPT1. *ChemBioChem 14*, 2029−2037.
(27) Case, D. A., Darden, T. A., Cheatham, T. E., III, Simmerling, C. L., Wang, J., Duke, R. E., Luo, R., Walker, R. C., Zhang, W., Merz, K. M., Roberts, B. P., Wang, B., Hayik, S., Roitberg, A., Seabra, G., Kolossváry, I., Wong, K. F., Paesani, F., Vanicek, J., Liu, J., Wu, X., Brozell, S. R., Steinbrecher, T., Gohlke, H., Cai, Q., Ye, X., Hsieh, M. J., Cui, G., Roe, D. R., Mathews, D. H., Seetin, M. G., Sagui, C., Babin, V., Luchko, T., Gusarov, S., Kovalenko, A., and Kollman, P. A. (2012) *AMBER11*, University of California, San Francisco.
(28) Jorgensen, W. L., Chandrasekhar, J., Madura, J. D., Impey, R. W., and Klein, M. L. (1983) Comparison of simple potential functions for simulating liquid water. *J. Chem. Phys. 79*, 926.
(29) Cornell, W. D., Cieplak, P., Bayly, C. I., Gould, I. R., Merz, K. M., Ferguson, D. M., Spellmeyer, D. C., Fox, T., Caldwell, J. W., and Kollman, P. A. (1996) A second generation force field for the simulation of proteins, nucleic acids, and organic molecules (vol 117, pg 5179, 1995). *J. Am. Chem. Soc. 118*, 2309.
(30) Wang, J. M., Wolf, R. M., Caldwell, J. W., Kollman, P. A., and Case, D. A. (2005) Development and testing of a general amber force field (vol 25, pg 1157, 2004). *J. Comput. Chem. 26*, 114.
(31) Elstner, M., Porezag, D., Jungnickel, G., Elsner, J., Haugk, M., Frauenheim, T., Suhai, S., and Seifert, G. (1998) Self-consistent-charge density-functional tight-binding method for simulations of complex materials properties. *Phys. Rev. B 58*, 7260−7268.
(32) Cui, G. L., Li, X., and Merz, K. M. (2007) Alternative binding modes in Orf2 catalyzed prenylation: Identification and validation. *Abstracts of Papers*, No. 233, American Chemical Society, Washington, DC.
(33) Yang, Y., Chakravorty, D. K., and Merz, K. M. (2010) Finding a Needle in the Haystack: Computational Modeling of Mg^{2+} Binding in the Active Site of Protein Farnesyltransferase. *Biochemistry 49*, 9658−9666.
(34) Yang, Y., Wang, B., Ucisik, M. N., Cui, G. L., Fierke, C. A., and Merz, K. M. (2012) Insights into the Mechanistic Dichotomy of the Protein Farnesyltransferase Peptide Substrates CVIM and CVLS. *J. Am. Chem. Soc. 134*, 820−823.
(35) Yang, Y., Miao, Y. P., Wang, B., Cui, G. L., and Merz, K. M. (2012) Catalytic Mechanism of Aromatic Prenylation by NphB. *Biochemistry 51*, 2606−2618.
(36) Bayly, C. I., Cieplak, P., Cornell, W. D., and Kollman, P. A. (1993) A Well-Behaved Electrostatic Potential Based Method Using Charge Restraints for Deriving Atomic Charges: The Resp Model. *J. Phys. Chem. 97*, 10269−10280.
(37) Frisch, M. J., Trucks, G. W., Schlegel, H. B., Scuseria, G. E., Robb, M. A., Cheeseman, J. R., Scalmani, G., Barone, V., Mennucci, B., Petersson, G. A., Nakatsuji, H., Caricato, M., Li, X., Hratchian, H. P., Izmaylov, A. F., Bloino, J., Zheng, G., Sonnenberg, J. L., Hada, M., Ehara, M., Toyota, K., Fukuda, R., Hasegawa, J., Ishida, M., Nakajima, T., Honda, Y., Kitao, O., Nakai, H., Vreven, T., Montgomery, J. A., Jr., Peralta, J. E., Ogliaro, F., Bearpark, M., Heyd, J. J., Brothers, E., Kudin, K. N., Staroverov, V. N., Kobayashi, R., Normand, J., Raghavachari, K., Rendell, A., Burant, J. C., Iyengar, S. S., Tomasi, J., Cossi, M., Rega, N., Millam, J. M., Klene, M., Knox, J. E., Cross, J. B., Bakken, V., Adamo, C., Jaramillo, J., Gomperts, R., Stratmann, R. E., Yazyev, O., Austin, A. J., Cammi, R., Pomelli, C., Ochterski, J. W., Martin, R. L., Morokuma, K., Zakrzewski, V. G., Voth, G. A., Salvador, P., Dannenberg, J. J., Dapprich, S., Daniels, A. D., Farkas, O., Foresman, J. B., Ortiz, J. V., Cioslowski, J., and Fox, D. J. (2009) *Gaussian 09*, revision A.02, Gaussian, Inc., Wallingford, CT.
(38) Darden, T., York, D., and Pedersen, L. (1993) Particle Mesh Ewald: An N.Log(N) Method for Ewald Sums in Large Systems. *J. Chem. Phys. 98*, 10089−10092.
(39) Essmann, U., Perera, L., Berkowitz, M. L., Darden, T., Lee, H., and Pedersen, L. G. (1995) A Smooth Particle Mesh Ewald Method. *J. Chem. Phys. 103*, 8577−8593.
(40) Sagui, C., Pedersen, L. G., and Darden, T. A. (2004) Towards an accurate representation of electrostatics in classical force fields: Efficient implementation of multipolar interactions in biomolecular simulations. *J. Chem. Phys. 120*, 73−87.
(41) Toukmaji, A., Sagui, C., Board, J., and Darden, T. (2000) Efficient particle-mesh Ewald based approach to fixed and induced dipolar interactions. *J. Chem. Phys. 113*, 10913−10927.
(42) Ryckaert, J.-P., Ciccotti, G., and Berendsen, H. J. C. (1977) Numerical integration of the cartesian equations of motion of a system with constraints: Molecular dynamics of n-alkanes. *J. Comput. Phys. 23*, 327−341.
(43) Miyamoto, S., and Kollman, P. A. (1992) SETTLE: An analytical version of the SHAKE and RATTLE algorithm for rigid water models. *J. Comput. Chem. 13*, 952−962.
(44) Pearlman, D. A., Case, D. A., Caldwell, J. W., Ross, W. S., Cheatham, T. E., Debolt, S., Ferguson, D., Seibel, G., and Kollman, P. (1995) Amber, a Package of Computer-Programs for Applying Molecular Mechanics, Normal-Mode Analysis, Molecular-Dynamics and Free-Energy Calculations to Simulate the Structural and Energetic Properties of Molecules. *Comput. Phys. Commun. 91*, 1−41.
(45) Case, D. A., Cheatham, T. E., Darden, T., Gohlke, H., Luo, R., Merz, K. M., Onufriev, A., Simmerling, C., Wang, B., and Woods, R. J. (2005) The Amber biomolecular simulation programs. *J. Comput. Chem. 26*, 1668−1688.
(46) http://www.ks.uiuc.edu/Research/vmd/, Version 1.9.1, February 4, 2012.
(47) Humphrey, W., Dalke, A., and Schulten, K. (1996) VMD: Visual molecular dynamics. *J. Mol. Graphics Modell. 14*, 33−38.
(48) http://gnuplot.info, Version 4.6.0, August 3, 2012.
(49) Jensen, M. O., Park, S., Tajkhorshid, E., and Schulten, K. (2002) Energetics of glycerol conduction through aquaglyceroporin GlpF. *Proc. Natl. Acad. Sci. U.S.A. 99*, 6731−6736.

(50) Crespo, A., Marti, M. A., Estrin, D. A., and Roitberg, A. E. (2005) Multiple-steering QM-MM calculation of the free energy profile in chorismate mutase. *J. Am. Chem. Soc. 127*, 6940−6941.
(51) Jarzynski, C. (1997) Nonequilibrium equality for free energy differences. *Phys. Rev. Lett. 78*, 2690−2693.
(52) Hummer, G., and Szabo, A. (2001) Free energy reconstruction from nonequilibrium single-molecule pulling experiments. *Proc. Natl. Acad. Sci. U.S.A. 98*, 3658−3661.
(53) Hummer, G., and Szabo, A. (2003) Kinetics from non-equilibrium single-molecule pulling experiments. *Biophys. J. 85*, 5−15.
(54) Grossfield, A. *WHAM: An implementation of the weighted histogram analysis method*, version 2.0.8, October 8, 2013 (http://membrane.urmc.rochester.edu/content/wham).
(55) Dougherty, D. A. (1996) Cation-π interactions in chemistry and biology: A new view of benzene, Phe, Tyr, and Trp. *Science 271*, 163−168.
(56) Dougherty, D. A. (2007) Cation-π interactions involving aromatic amino acids. *J. Nutr. 137*, 1504S−1508S.
(57) Jenson, C., and Jorgensen, W. L. (1997) Computational investigations of carbenium ion reactions relevant to sterol biosynthesis. *J. Am. Chem. Soc. 119*, 10846−10854.
(58) Hong, Y. J., and Tantillo, D. J. (2013) C-H$\cdots\pi$ interactions as modulators of carbocation structure: Implications for terpene biosynthesis. *Chem. Sci. 4*, 2512−2518.
(59) Hawkins, G. D., Cramer, C. J., and Truhlar, D. G. (1995) Pairwise Solute Descreening of Solute Charges from a Dielectric Medium. *Chem. Phys. Lett. 246*, 122−129.
(60) Hawkins, G. D., Cramer, C. J., and Truhlar, D. G. (1996) Parametrized models of aqueous free energies of solvation based on pairwise descreening of solute atomic charges from a dielectric medium. *J. Phys. Chem. 100*, 19824−19839.
(61) Srinivasan, J., Cheatham, T. E., Cieplak, P., Kollman, P. A., and Case, D. A. (1998) Continuum solvent studies of the stability of DNA, RNA, and phosphoramidate: DNA helices. *J. Am. Chem. Soc. 120*, 9401−9409.
(62) Weiser, J., Shenkin, P. S., and Still, W. C. (1999) Approximate atomic surfaces from linear combinations of pairwise overlaps (LCPO). *J. Comput. Chem. 20*, 217−230.